UCRL-8279

Cy. 2

# UNIVERSITY OF CALIFORNIA

## Ernest O. Lawrence Radiation Laboratory

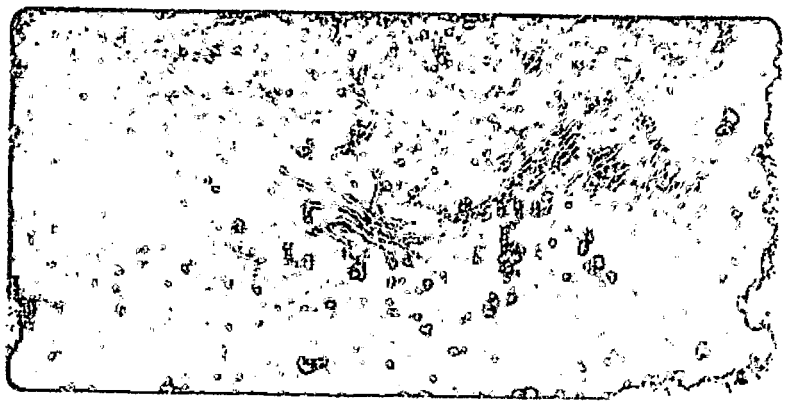

BERKELEY, CALIFORNIA

## DISCLAIMER

This document was prepared as an account of work sponsored by the United States Government. While this document is believed to contain correct information, neither the United States Government nor any agency thereof, nor the Regents of the University of California, nor any of their employees, makes any warranty, express or implied, or assumes any legal responsibility for the accuracy, completeness, or usefulness of any information, apparatus, product, or process disclosed, or represents that its use would not infringe privately owned rights. Reference herein to any specific commercial product, process, or service by its trade name, trademark, manufacturer, or otherwise, does not necessarily constitute or imply its endorsement, recommendation, or favoring by the United States Government or any agency thereof, or the Regents of the University of California. The views and opinions of authors expressed herein do not necessarily state or reflect those of the United States Government or any agency thereof or the Regents of the University of California.

UCRL-8279

cy 2

UNIVERSITY OF CALIFORNIA

Radiation Laboratory
Berkeley, California

Contract No. W-7405-eng-48

# ANTIPROTON-PROTON CROSS SECTIONS AT 133, 197, 265, AND 333 Mev

Charles A. Coombes, Bruce Cork, William Galbraith,
Glen R. Lambertson, and William A. Wenzel

June 30, 1958

Printed for the U. S. Atomic Energy Commission

# ANTIPROTON-PROTON CROSS SECTIONS AT 133, 197, 265, AND 333 Mev

Charles A. Coombes, Bruce Cork, William Galbraith, Glen R. Lambertson, and William A. Wenzel

Radiation Laboratory
University of California
Berkeley, California

June 30, 1958

## ABSTRACT

In a scintillation-counter experiment the interaction of antiprotons with protons in the energy region 133 to 333 Mev has been studied. Antiprotons, produced internally in the Bevatron, channeled externally by a system of magnetic quadrupoles and bending magnets, and identified by time of flight, entered a target containing liquid hydrogen. This target was completely surrounded by a system of scintillation counters which detected both scattered antiprotons and annihilation secondaries. An electrostatic-magnetic velocity spectrometer was used in the external magnetic channel to increase the ratio of antiprotons to pions. The $\bar{p}$-p total, elastic, inelastic, and charge-exchange cross sections and the angular distribution of elastic scattering were measured at each energy. The inelastic cross section is approximately one-half the total cross section at these energies. The results are discussed in connection with current theories.

# ANTIPROTON-PROTON CROSS SECTIONS AT 133, 197, 265, AND 333 Mev*

Charles A. Coombes, Bruce Cork, William Galbraith,†
Glen R. Lambertson, and William A. Wenzel

Radiation Laboratory
University of California
Berkeley, California

June 30, 1958

## INTRODUCTION

Accurate measurements of antiproton-proton cross sections are of considerable importance in the development of a theory of nuclear forces. Difficulties encountered in obtaining antiproton beams of high intensity and purity have limited the scope of experiments with these particles. In previous experiments the total $\bar{p}$-p cross section has been measured for energies in the range 190 to 700 Mev,[1] the inelastic cross section has been measured at 450 Mev,[2] and the elastic scattering has been measured at lower energies.[3, 4]

The purpose of the experiment presented here was to measure simultaneously and with improved precision the $\bar{p}$-p total, elastic, inelastic, and charge-exchange cross sections as a function of energy. An intermediate-energy region was selected for study because of current theoretical interest. Because the yield of antiprotons is low at low energies, the hydrogen target was made as thick as possible consistent with the requirement that the antiprotons scattered at large angles have sufficient energy to escape the target. With the single experimental arrangement used the maximum energy was determined by the strength of the magnets in the beam channel.

*Work done under the auspices of the U. S. Atomic Energy Commission.

†Commonwealth Fellow. On leave of absence from Atomic Energy Research Establishment, Harwell, England.

## ANTIPROTON BEAM

The antiproton beam developed for this experiment was similar to that used in earlier counter experiments,[1] but had the following important additional advantages.

1. Use of a larger-aperture quadrupole system, together with the increase of Bevatron beam intensity during the past 18 months, gave nearly an order-of-magnitude increase in the flux of the external negative beam containing the antiprotons.

2. An electrostatic-magnetic velocity spectrometer reduced the background of fast particles in the beam without reducing the antiproton intensity.

3. The provision of several internal targets made it unnecessary to relocate the external magnetic system for each momentum.

4. The normal shift in channel momentum as the Bevatron field increased during the 50-millisecond beam pulse was offset by a pulsed correcting magnet.

5. To avoid loss of particles near the edges of the momentum interval, the momentum dispersion effected by the Bevatron field was subsequently canceled by a large bending magnet.

Figure 1 shows the over-all arrangement of the antiproton channel. Separate internal targets were used for each of the four momenta; only one is shown in the figure. Targets were of beryllium measuring 1/2 by 3/8 inch by 6 inches long. Each target was so located that negative particles of the desired momentum were selected in the forward direction; in this way the antiproton yield was at a maximum and the apparent source size was a minimum. After a steering correction was applied with deflecting magnet $C_1$, an 8-inch-aperture quadrupole set $Q_1$ focused the beam onto a 2-by-8-inch horizontal collimating slit at the entrance to the quadrupole set $Q_2$. The velocity spectrometer was set to give no deflection to the antiprotons, which then passed through the slit. Fast particles in the beam were deflected vertically 1 to 3 inches, depending on the momentum. Most of these fast particles struck the edge of the slit and were absorbed or degraded sufficiently so that they were removed from the beam by the deflecting magnet H. The momentum width of the beam, about ± 5%, was determined by the horizontal width of the collimating slit and the dispersion produced

by the Bevatron field. $Q_2$ acted as a field lens, redirecting particles of different momenta toward the center of the deflecting magnet H, where the large deflection of $45^{\circ}$ served both to determine accurately the average momentum selected and to direct particles of different momenta along the axis of the following iterated 4-inch-aperture quadrupole system ($Q_3 - Q_6$).

On the basis of previous experience the length of the 4-inch system was made sufficient for identification of antiprotons by time of flight at the highest energy to be studied. Improved time resolution in new photomultiplier tubes made this length more than adequate. Magnet $C_2$ deflected the beam $6^{\circ}$ in order to eliminate positive protons produced as secondaries in the channel.

Figure 2 shows schematically how particles of different momenta behave in the beam channel. The transition (without appreciable beam loss) from the 8-inch to the 4-inch system was aided by several factors. Excursions in the vertical direction after the focus at the slit were kept small by the focusing in $Q_2$ and in the deflecting magnet. Canceling the momentum dispersion at deflecting magnet H minimized the horizontal aperture required beyond that point. The 4-inch lenses were spaced relatively closely to permit the transmission of particles with rather large angular divergences. This large angular acceptance also served to contain the Coulomb scattering introduced by the time-of-flight counters, especially at low momenta.

Some loss of antiprotons occurred at the slit because of Coulomb scattering in the 0.060-inch stainless steel vacuum wall of the Bevatron. Losses due to this effect were estimated to have reduced the antiproton intensity by at least a factor of two at the lowest momentum studied (600 Mev/c). Helium bags extending from the exit of the Bevatron to the spectrometer and from the spectrometer to the exit of $Q_3$ displaced the air in order to minimize scattering in the region ahead of the time-of-flight counters.

A thin-foil technique similar to that described previously[1] was used to direct the circulating proton beam of the Bevatron onto the internal target. In this way a beam pulse largely free of radiofrequency bunching as well as synchrotron and magnetic field ripple was obtained.

The length of the beam pulse was about 50 milliseconds, and during this time the Bevatron field changed enough to introduce a significant

variation in the momentum of particles going toward the external beam channel. To offset this effect the beam was directed through a special compensator $C_0$ just ahead of $C_1$ (Fig. 1). This consisted of pole tips mounted on the return yoke of the Bevatron magnet in such a way as to direct stray return flux from the Bevatron across the beam trajectory. This field varied more rapidly than and in the direction opposite to that in the Bevatron gap. In this way the variation of the average momentum of particles directed down our channel was reduced from 3% to less than 1% during the 50-millisecond period.

Table I gives the yields of antiprotons and fast particles ($\pi$ mesons) measured at the end of the magnetic channel. No corrections have been made for Coulomb scattering or decay in flight.

## VELOCITY SPECTROMETER

The velocity spectrometer is of the parallel-plate type in which crossed electric and magnetic fields are used to select, by null deflection, charged particles of a given velocity. The device consists of two electrodes, 8 inches in width and 19 feet in length, within a vacuum enclosure, $1.5 \times 1.5 \times 20$ feet, around which are wound magnetizing coils. The particle beam enters and leaves the enclosure through thin, 0.012-inch, aluminum windows 8 inches in diameter. The electrodes are of 0.002-inch stainless steel stretched across a frame of 2-inch-o.d. stainless steel tubing. They are separated by a gap of $6\frac{1}{2}$ inches at the entrance end, tapering to 2 inches at the exit in order to accommodate with little loss of aperture a converging beam from an 8-inch quadrupole lens while producing the maximum separation for a given voltage. In normal operation a gap voltage of 300 kv was maintained with the plates oppositely charged with respect to ground; corresponding magnetic fields were of the order of 100 gauss. With more careful electrode fabrication and a better vacuum system the voltage gradient can probably be increased considerably.

In operation a particle of velocity $\beta_0$ is selected by adjustment of the magnetic field B so as to give $\beta_0 = E/B$ with average electric field E. Particles of velocity $\beta_0$ are passed with no net deflection, while others are displaced at the output of the spectrometer by a distance

Table I. Beam Characteristics

The momentum band width is ± 5%. Yields per proton incident on the 6" beryllium target were measured at the exit of the magnetic channel and correspond to operation with the spectrometer off. Operation of the spectrometer at 300 kv rejects fast particles by the factor shown.

| Average momentum (Mev/c) (± 3%) | Angle of emergence from target (degrees) | Solid angle ($10^{-3}$ sterad) | $\bar{p}/p$ ($10^{-12}$±20%) | $\pi^-/p$ ($10^{-6}$±40%) | $\bar{p}/\pi^-$ ($10^{-6}$±50%) | Spectrometer rejection factor (±20%) |
|---|---|---|---|---|---|---|
| 600 | 0 | 2.2 | 6 | 4 | 1.5 | 30 |
| 700 | 0 | 1.8 | 12 | 5 | 2.4 | 10 |
| 800 | 0 | 1.6 | 22 | 5 | 4.4 | 7 |
| 900 | 7 | 1.4 | 48 | 6 | 8 | 4 |

Table I. Beam Characteristics

The momentum band width is ± 5%. Yields per proton incident on the 6" beryllium target were measured at the exit of the magnetic channel and correspond to operation with the spectrometer off. Operation of the spectrometer at 300 kv rejects fast particles by the factor shown.

| Average momentum (Mev/c) (± 3%) | Angle of emergence from target (degrees) | Solid angle ($10^{-3}$ sterad) | $\bar{p}/p$ ($10^{-12}$±20%) | $\pi^-/p$ ($10^{-6}$±40%) | $\bar{p}/\pi^-$ ($10^{-6}$±50%) | Spectrometer rejection factor (±20%) |
|---|---|---|---|---|---|---|
| 600 | 0 | 2.2 | 6 | 4 | 1.5 | 30 |
| 700 | 0 | 1.8 | 12 | 5 | 2.4 | 10 |
| 800 | 0 | 1.6 | 22 | 5 | 4.4 | 7 |
| 900 | 7 | 1.4 | 48 | 6 | 8 | 4 |

$$y = \frac{e\ell^2 E}{2pc} \left[\frac{1}{\beta_0} - \frac{1}{\beta}\right] \tag{1}$$

and have an angular deflection

$$\theta = \frac{e\ell E}{pc} \left[\frac{1}{\beta_0} - \frac{1}{\beta}\right] , \tag{2}$$

where $\beta$ is the velocity of the deflected particle of momentum $p$ and charge $e$, and $\ell$ is the effective length of the spectrometer.

Figure 3 shows how the fluxes of detected antiprotons and fast particles in the beam varied as a function of magnetic field in the spectrometer for a fixed electric field. The vertical width of the target was made small, so that its magnified image contributed little to the beam width at the slit. Much of the observed width of the beam is accounted for by Coulomb scattering in the stainless steel vacuum wall of the Bevatron. In spite of this scattering, the separation factor achieved in this experiment was much greater at lower momenta, as shown in Table I. This is expected for two reasons. First, as Eqs. (1) and (2) show, the separation is a sensitive function of momentum. Second, the muon contamination of the separated beam is less at low momenta because of the greater spread in laboratory angle of emission in $\pi$ decay.

## HYDROGEN TARGET

A specially constructed thin-walled liquid hydrogen target was used in the cross-section measurements (see Fig. 4). The hydrogen flask was of stainless steel 0.010 inch thick. In the evacuated space surrounding the flask was a thin (0.003-inch) copper heat shield at liquid nitrogen temperature. The outer vacuum wall, at room temperature, was made thin over a large solid angle in the forward direction, so that antiprotons scattered at angles up to $60^\circ$ in the laboratory could escape. Finally, the target was constructed in such a way that scintillation counters could surround the whole structure. This was necessary because annihilation and scattering events could be distinguished reliably only by means of a detector having large solid angle.

## DETECTION OF INTERACTIONS

Figure 4 shows the hydrogen target surrounded by plastic scintillation counters. These counters were divided into three groups. The forward counter t measured transmitted antiprotons and corresponded to the good-geometry detector of the standard attenuation experiment. Ten s counters, $S_1$ through $S_5$, a left and a right half for each of five zones, detected scattered antiprotons as well as annihilation secondaries. Finally, the a counters, which detected mainly annihilation secondaries emitted in the backward direction, covered the sides and entrance face of the hydrogen target. A $\frac{1}{2}$-inch-thick layer of lead (not shown in Fig. 4) was placed between the hydrogen target and the a counters. This thickness was estimated to be the optimum for conversion of $\gamma$ rays from $\pi^0$ mesons formed in annihilation without appreciable attenuation of the charged $\pi$ mesons. With the exception of the entrance a counter, which was 1 inch thick, all the counters were of 1/4-inch plastic sheet.

## ELECTRONICS

A block diagram of the basic electronics is shown in Fig. 5. Six 1/4-inch-thick plastic scintillation counters of area 4 by 4 inches were used to identify antiprotons by time of flight over the 30-foot distance from the exit of $Q_3$ to the exit of $Q_6$. The associated electronic circuits were similar to those used previously.[1] There were two important differences. First, the photomultipliers were type RCA C7251 instead of RCA 6810. The newer tubes with spherical cathode surfaces were found to give appreciably better time resolution. These tubes have a more uniform transit time from the surface of the photocathode. Therefore, a larger-diameter light pipe was used to give increased photon-collection efficiency. Second, a time-of-flight anticoincidence was added. That is, an additional signal from counter A, the first time-of-flight counter, was timed for fast particles ($\beta \approx 1$) and introduced in anticoincidence into one of the intermediate coincidence circuits. This is particularly effective in the suppression of accidental coincidences. It can be used to reject fast particles whenever the time-of-flight difference between slow and fast particles is longer than the pulse length produced by a slow particle in the first counter. Figure 6 shows delay curves measured for 700-Mev/c particles with and without the

anticoincidence in operation. The peaks show clear separation of $K^-$ mesons and antiprotons. At each energy contamination of the antiproton beam is estimated to be less than 1% and has been neglected in all cross-section calculations.

For each antiproton detected a fast gate ($2 \times 10^{-8}$ sec) was produced; this was mixed with each of the signals from the counters surrounding the hydrogen target. The gated signals were inserted at intervals along two transmission lines, added with opposite polarity, displayed on a Tektronix-517 oscilloscope, and photographed. The oscilloscope sweep was triggered each time an antiproton entered the hydrogen target. Any one or more of the seventeen pulses shown schematically in Fig. 7a appears on the oscilloscope trace. The first pulse is the gate itself. The next three pulses are from a three-channel chronotron which gives an accurate measurement of the antiproton time of flight. Next are the a and t pulses followed by pulses from each of the ten scattering counters. Finally the s pulse appears if there is a pulse in any of the scattering counters. Figure 7b shows several traces taken from the 35-mm film that recorded the data. Parallel outputs from the gating circuit furnished pulses so that counts in t, a, and s as well as the coincidences as, at, st could be recorded on scalers. In this way the performance of the electronics could be monitored continuously.

## ANALYSIS OF DATA

At each energy, a number of runs was made with and without liquid hydrogen in the target. The $\bar{p}$-p cross sections were obtained by a difference method. Since only 10 to 25% of the antiprotons interacted in the hydrogen and the target material, most antiprotons were detected simply as a transmission, a count in t only. Other events were tentatively classified as follows. A count in only one s counter was a scattering; a count in only two s counters was either elastic or inelastic scattering depending upon whether or not the included angle between the two counters was consistent with the kinematics of an elastic scattering event in which both scattered and recoil particles were detectable. A count in a or in more than two s counters was an inelastic event. Finally, an event in which none of the counters surrounding the hydrogen target counted was classified as a charge exchange.

## CORRECTIONS, RESULTS, AND UNCERTAINTIES

Figures 8 through 10 show the experimental results along with cross sections obtained from related experiments. Table II summarizes our results and indicates some of the corrections required. The forward-scattering correction $\Delta\sigma_0$ was obtained from the "optical theorem"[5] in terms of the measured total cross section $\sigma_T$,

$$\Delta\sigma_0 = \Delta\Omega_0 \, (k\sigma_T/4\pi)^2. \tag{3}$$

Here $\Delta\Omega_0$ is the solid angle subtended at the hydrogen target by the t counter and k is the antiproton wave number.

When a scattered particle emerged in the large-angle region covered by the a counters it had low energy and was absorbed in the target and surrounding material. If this backward scattered particle was the antiproton, its annihilation was detected, and these events were indistinguishable from normal annihilations. For this reason, there was a maximum angle (see Table II) beyond which antiproton scatterings could not be measured in this experiment.

In about 10% of all scattering events both scattered particles were detected. Because we cannot tell which particle was the antiproton, we have arbitrarily assigned half an event to each of the angular zones in which a count occurred. As predicted from considerations of counter geometry, 80% of all scattering events detected in $S_5$, and smaller amounts for the other counters, were of this type. Therefore, we do not know in detail the angular distribution above and just below $90^\circ$ (c.m.).

In correcting for large-angle scattering we have assumed that at each energy the angular distribution is of the same shape as that obtained from the phase shifts at 140 Mev calculated by Ball and Chew.[6, 7]

There is a possibility that some annihilation events were classified as elastic scattering or charge exchange. In estimating that such cases were infrequent, we have considered the characteristics of the annihilation process measured here and elsewhere,[8, 9] together with the high detection efficiency of our counter system for both charged particles and $\gamma$ rays. Another estimate of the contamination of the charge-exchange events by annihilations was obtained from the results of a separate experiment. With

Table II. Antiproton-proton cross sections

| Kinetic energy (Mev) | Total cross section (mb) | Observed elastic cross section (mb) | Minimum cutoff angle (degrees, c.m.) | Maximum cutoff angle (degrees, c.m.) | Forward scattering correction (mb) | Backward scattering correction (mb) | Corrected elastic cross section (mb) | Charge-exchange cross section (mb) | Inelastic cross section (mb) |
|---|---|---|---|---|---|---|---|---|---|
| 133 ± 13 | 166 ± 8 | $59^{+6}_{-8}$ | 14 | 93 | 7 | 6 | $72^{+9}_{-11}$ | $10^{+2}_{-3}$ | $84^{+14}_{-12}$ |
| 197 ± 16 | 152 ± 7 | $53^{+5}_{-7}$ | 14 | 119 | 8 | 3 | $64^{+7}_{-9}$ | $11^{+2}_{-4}$ | $77^{+12}_{-10}$ |
| 265 ± 17 | 124 ± 7 | $39^{+4}_{-5}$ | 14 | 120 | 8 | 3 | $50^{+6}_{-7}$ | $8^{+2}_{-3}$ | $66^{+10}_{-9}$ |
| 333 ± 17 | 114 ± 4 | $38^{+3}_{-4}$ | 14 | 121 | 8 | 3 | $49^{+5}_{-7}$ | $7^{+2}_{-2}$ | $58^{+8}_{-7}$ |

incident antiprotons of momentum 600 Mev/c, a thick target of lead (and later of aluminum) was placed behind the empty hydrogen target (see Fig. 4). With this arrangement all incident antiprotons annihilated within the space enclosed by counters, and the annihilation-detection efficiency was observed to be high, 97% for lead (98.5% for aluminum).

For the charge-exchange events the angular distribution is not known. Antineutrons produced at large angles have relatively low energy and are absorbed with fairly high probability in the heavy material surrounding the hydrogen target. The charge-exchange cross sections presented in Fig. 8 and in Table II have been corrected, with the assumption that the antineutrons are scattered predominantly forward (into the s counters). If the angular distribution is nearly symmetric in the center-of-mass system, as is predicted by the calculations of Fulco,[7] then these cross sections should be increased by about one-fourth.

The following outline contains a summary of experimental uncertainties and of the corrections applied in arriving at the experimental values for each cross section. Because most of the corrections and uncertainties were only slightly energy-dependent, average values are given.

(1) All cross sections

(a) a count in a in accidental coincidence with antiproton: $1\frac{1}{2} \pm 1\%$

(b) uncertainty in number of hydrogen atoms per square centimeter: $\pm 2\%$

(2) Total cross section

(a) statistical uncertainty: $\pm 4\%$

(b) forward scattering into t counter: $5 \pm 1\%$

(3) Elastic scattering cross section

(a) statistical uncertainty: $\pm 8\%$

(b) measured counter inefficiency: $0^{+1}_{-0}\%$

(c) scattering through gaps between s counters: $4 \pm 2\%$

(d) scattered antiprotons that annihilated in detectors and surrounding materials: $8 \pm 4\%$

(e) forward scattering into t counter: $12 \pm 2\%$

(f) annihilation of backward scattered antiprotons: $6 \pm 4\%$

(g) annihilations that simulated scattering events: $0^{+0}_{-6}\%$

(h) plural scattering: $5 \pm 1\%$. A correction was also applied to the angular distribution.

(4) Charge-exchange cross section

(a) statistical uncertainty: $\pm 17\%$

(b) elastic scattering through gaps between s counters: $20 \pm 10\%$

(c) undetected annihilations: $0^{+0}_{-25}\%$

(d) annihilation of antineutrons in detectors and surrounding material: $6 \pm 4\%$.

(5) Inelastic cross section

(a) reflects the corrections and uncertainties of the other cross-section measurements.

## DISCUSSION

In Figs. 8 and 10 the $\bar{p}$-p total, elastic, and inelastic cross sections show similar dependence upon energy. The total cross section agrees with previous results.[1] The values of the total cross section, Fig. 8, have an inverse velocity dependence over the energy range measured. The inelastic cross section is one-half and the charge exchange is about 7% of the total. The angular distribution at each energy, as is shown in Fig. 9, is peaked strongly forward, suggesting diffraction scattering from a strongly absorptive interaction.

Recently several models have been proposed to account for the observed antinucleon-nucleon inelastic and elastic cross sections. The semi-phenomenological model by Ball and Chew[6] is applicable in the range of energies studied here. The essential feature of this model is the use of the Yukawa formalism and a potential that correctly describes the experimental nucleon-nucleon interaction at these energies. The annihilation interaction is attributed to a short-range absorbing core, and the W.K.B. approximation is used to calculate the phase shifts and to estimate the probability of absorption for each partial wave. In this way both annihilation and scattering cross sections are obtained. From the calculated phase shifts, Fulco has obtained the angular distribution for the $\bar{p}$-p elastic scattering and charge-exchange interactions at 140 Mev.[7] The predictions are in good agreement with our measurements (Figs. 9a and 10).

The phenomenological model of Koba and Takeda[10] also divides the region of antinucleon-nucleon interaction into two parts, an absorbing core and a surrounding meson cloud. The most appealing feature of this model

is that it seems to account for the high multiplicity of pions and low multiplicity of K mesons observed in antinucleon-nucleon annihilation. In analogy with the continuum theory applied by Feshbach and Weisskopf to the absorption of neutrons,[11] antinucleon-nucleon absorption and scattering cross sections are obtained for an interaction which is completely absorbing inside a volume of radius $r_0$. The absorption cross section is given approximately by the relation $\sigma_a = \pi (r_0 + \lambda\!\!\!^{-})^2$, where $\lambda\!\!\!^{-}$ is the center-of-mass wave length of the antiproton. The energy dependence of $\sigma_a$ shown in Fig. 10 is in good agreement for $r_0 = (0.90 \pm .05) \times 10^{-13}$ cm. Koba and Takeda have pointed out that the rather large "core" radius required to explain the observed annihilation cross section is approximately equal to the nucleon "size" as determined by high-energy electron-proton scattering.[12] Measurements with high-energy protons and pions give a similar "size."[13, 14] For the annihilation process this size is not obviously applicable, although Tamm[15] has given reasons for expecting that the effects of an extended "core" should be observed in antinucleon-nucleon annihilation. Ball and Chew find that in this intermediate energy range the magnitude of the annihilation cross section is insensitive to the assumed radius at which complete absorption occurs. In their model the probability of annihilation is determined almost entirely by the meson forces. It is expected that a greater knowledge of the nature of the nucleon core can be obtained from measurements of the annihilation cross section at high energies.

The experimental results are suggestive of the classical "black sphere" interaction, for which the absorption and elastic cross sections are each half the total. The solid curves of Fig. 9 were obtained from optical-model considerations. This angular distribution of elastic scattering is given by

$$\frac{d\sigma}{d\Omega} = k^2 R^4 \left[ \frac{J_1 (2kR \sin \theta/2)}{2kR \sin\theta/2} \right]^2 , \qquad (4)$$

where the effective radius R is determined from the total cross section by $2\pi R^2 = \sigma_T$.

We attach no special significance to the good fit of these curves to the experimental angular distributions, except to note that almost any model that predicts the measured annihilation and elastic-scattering cross

sections may be expected to give fair agreement with the observed angular distribution. The forward scattering calculated by Fulco is about 10% above the minimum given by the "optical theorem" for a purely absorptive interaction. The large-angle elastic scattering where our measurements were least precise is relatively sensitive to the amount of potential scattering in the interaction. This can be seen from a comparison of the solid and dashed curves of Fig. 9a. Similarly, the charge-exchange scattering is expected to be relatively sensitive to details of the model used to describe the interaction.

The Ball-Chew model predicts an irregularity in the energy dependence of the $\bar{p}$-p absorption cross section at each energy for which the top of the potential barrier is reached by a partial wave. Since our measurements are more accurate for the total than for the absorption cross section, we have looked particularly for irregularities in the behavior of the total cross section as a function of energy. Using the information given by the chronotron, we have divided the data at each energy into three subgroups of different energies. Figure 10 shows the total cross sections measured in this way at each of twelve energies.

## ACKNOWLEDGMENTS

We wish to express our appreciation to Dr. Edward J. Lofgren and the Bevatron operating crew. The spectrometer was designed and developed by George Edwards and Emery Zajec. The liquid hydrogen target was designed by Dr. LeRoy Kerth, the late Robert Mathewson, and Roy S. Hickman. The large assortment of plastic scintillators and light pipes were designed and constructed by Don Bliss and Robert Luedtke of the Accelerator Technician Shop. A considerable part of the special electronics was developed by Fred H. G. Lothrop. The film scanning was done by William Wadman and James Peck.

## REFERENCES


1. Cork, Lambertson, Piccioni, and Wenzel, Phys. Rev. 107, 248 (1957).
2. Chamberlain, Keller, Mermod, Segrè, Steiner, and Ypsilantis, Phys. Rev. 108, 1553 (1957).
3. Agnew, Elioff, Fowler, Gilly, Lander, Oswald, Powell, Segrè, Steiner, White, Wiegand, and Ypsilantis, $\bar{p}$-p Elastic and Charge-Exchange Scattering at about 120 Mev, UCRL-8231, Mar. 1958.
4. Goldhaber, Kalogeropoulos, and Silberberg, Antiproton-Hydrogen Scattering and Inelastic Scattering from Complex Nuclei (to appear as Letter to the Editor of Physical Review).
5. H. A. Bethe and F. de Hoffman, Mesons and Fields (Row, Peterson, New York, 1950) Vol. II, p. 76.
6. J. S. Ball and G. F. Chew, Phys. Rev. 109, 1395 (1958).
7. Jose R. Fulco, Phys. Rev. 110, 784 (1958).
8. Barkas, Birge, Chupp, Ekspong, Goldhaber, Goldhaber, Heckman, Perkins, Sandweiss, Segrè, Smith, Stork, and van Rossum, Amaldi, Buroni, Castagnoli, Franzinetti, and Manfredini, Phys. Rev. 105, 1037 (1957).
9. Brabant, Cork, Horwitz, Moyer, Murray, Wallace, and Wenzel, Phys. Rev. 102, 1622 (1956).
10. Z Koba and G. Takeda, Progr. Theoret. Phys. 19, 269 (1958).
11. H. Feshback and V. F. Weisskopf, Phys. Rev. 76, 1550 (1949).
12. E. E. Chambers and R. Hofstadter, Phys. Rev. 103, 1454 (1956).
13. W. Rarita, Phys. Rev. 104, 221 (1956); Cork, Wenzel, and Causey, Phys. Rev. 107, 859 (1957).
14. Cronin, Cool, and Abashian, Phys. Rev. 107, 1121 (1957); Walker, Hushfar, and Shepard, Phys. Rev. 104, 526 (1956); Cool, Piccioni, and Clark, Phys. Rev. 103, 1082 (1956); Maenchen, Powell, Saphir, and Wright, Phys. Rev. 99, 1619 (1955).
15. I. E. Tamm, Soviet Physics (JETP) 5, 154 (1957).

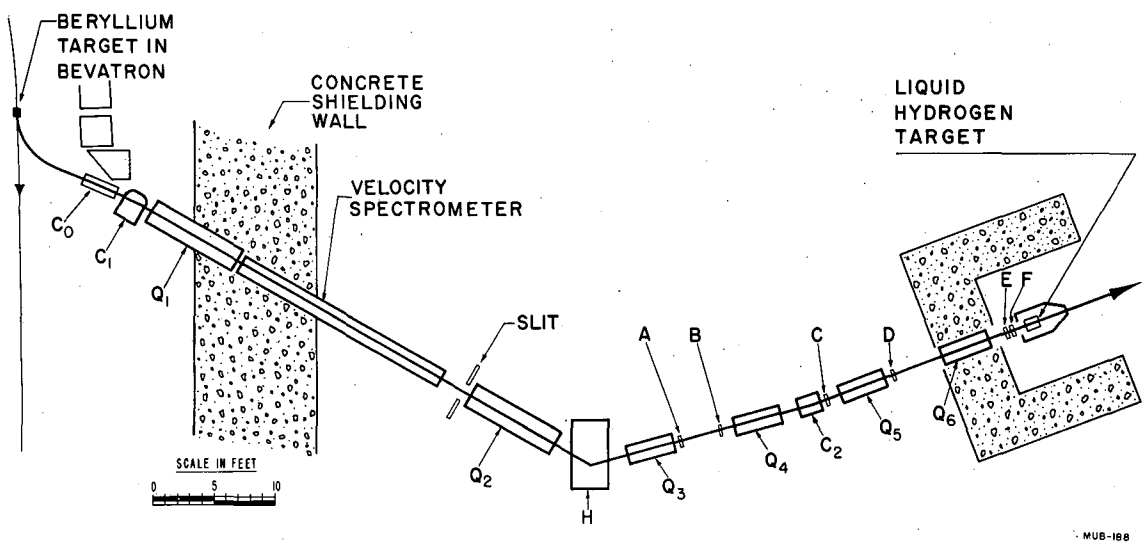


Fig. 1. Experimental arrangement. Compensator $C_0$ corrects for changes in the Bevatron field. $C_1$, $C_2$, and H are deflecting magnets. Quadrupole sets $Q_1$ and $Q_2$ have 8-inch aperture. $Q_3$—$Q_6$ have 4-inch aperture. Counters A through F are 4-by-4-by-1/4-inch plastic scintillators used for time-of-flight measurement.

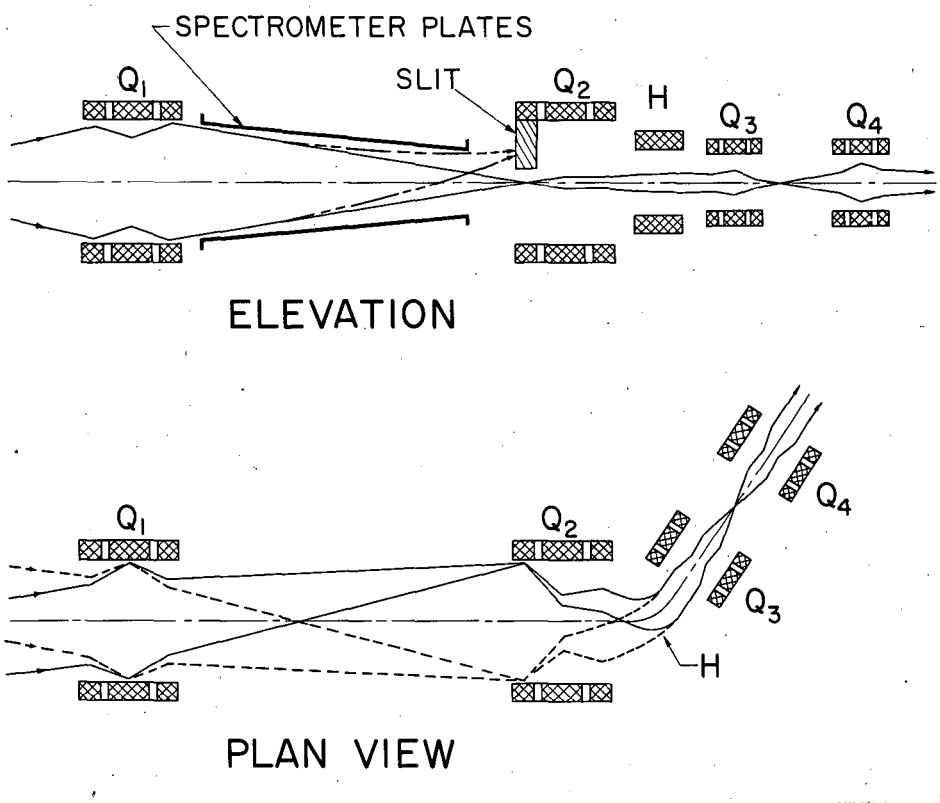


Fig. 2. Optical properties of the magnetic system (schematic). The solid and dashed lines in the plan view represent particles of low and high momenta, respectively, after dispersion by the Bevatron field. The effects of chromatic aberration have been neglected. The elevation view shows how fast particles in the beam (striking slit) were separated from antiprotons (undeflected) by the velocity spectrometer.

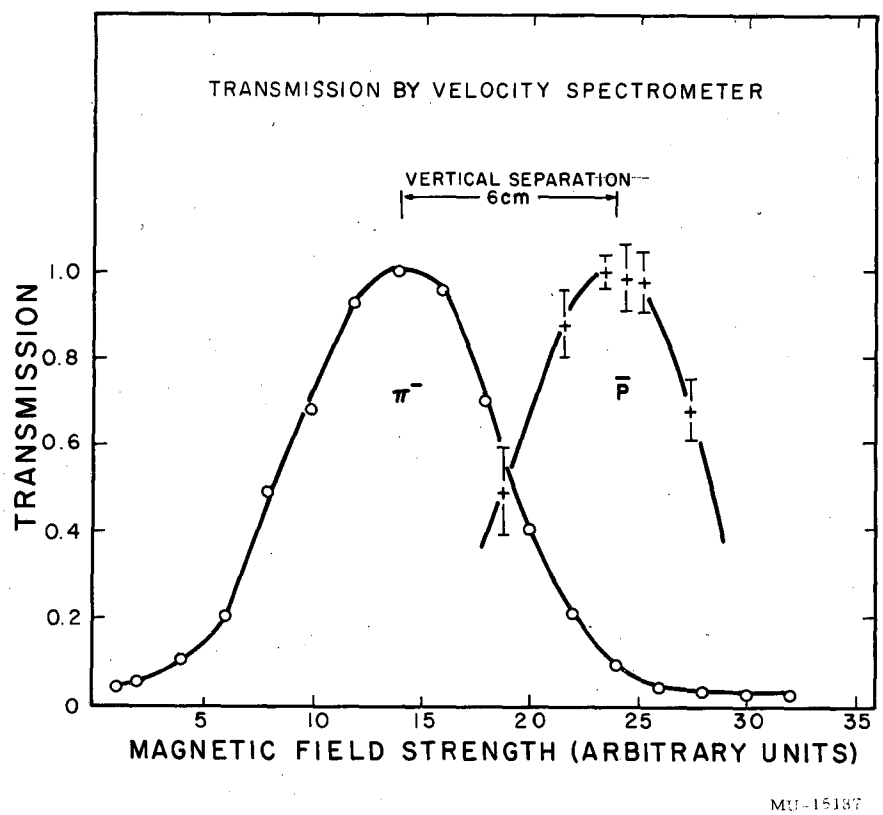


Fig. 3. Relative transmission by the spectrometer at 700 Mev/c of antiprotons and of fast particles. The spectrometer was operated with a gap voltage of 300 kv. Each curve is separately normalized to unity. The observed widths are largely accounted for by Coulomb scattering in the vacuum wall of the Bevatron.

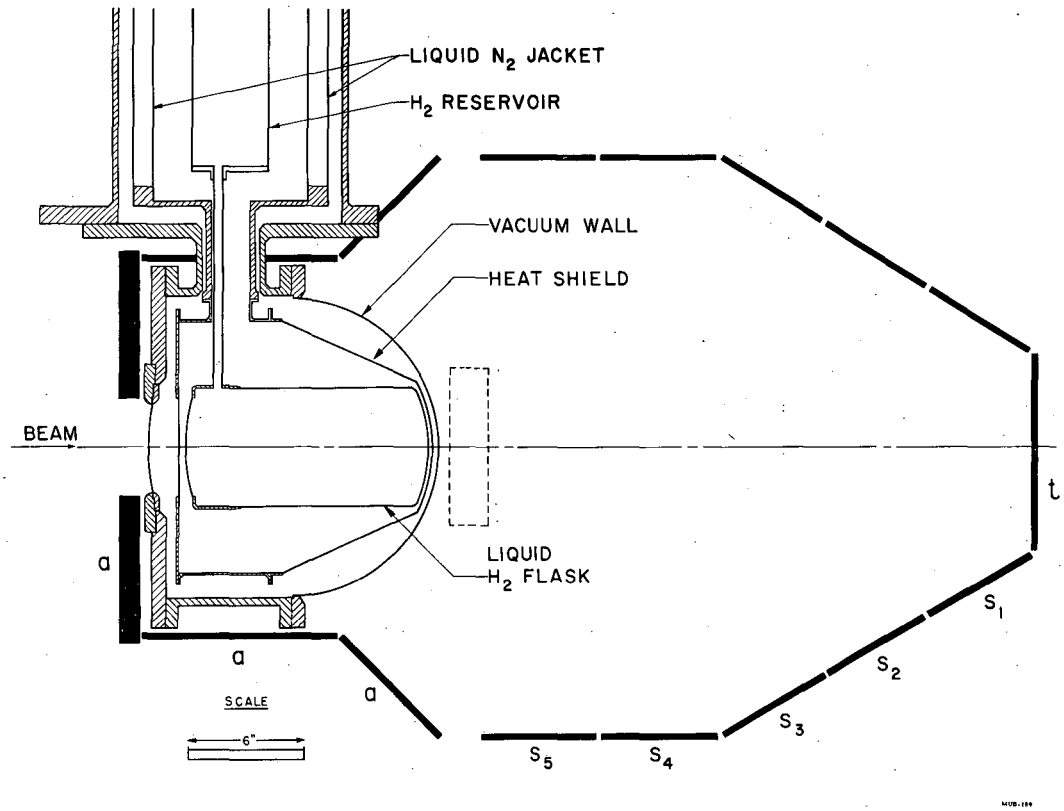


Fig. 4. Liquid hydrogen target and surrounding counters. The target flask of 0.010-inch stainless steel was surrounded by a 0.003-inch copper heat shield and a 0.040-inch aluminum vacuum wall in the forward direction (gasket details are not shown); a, t and $S_1$ through $S_5$ were plastic scintillation counters. The dashed rectangle shows position of an absorber of lead or aluminum when used in an experiment to measure annihilation detection efficiency.

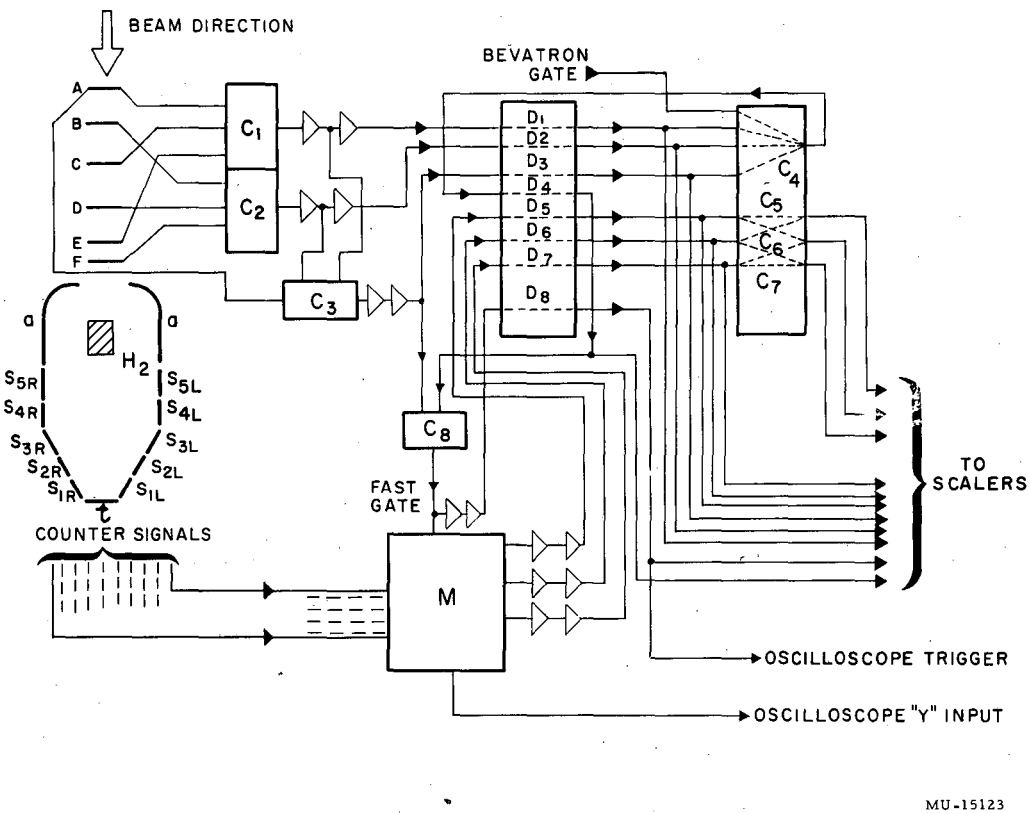


Fig. 5. Block diagram of basic electronics. A through F are time-of-flight scintillation counters; a, t, and $S_1 - S_5$ are scintillation counters that detected the interactions of antiprotons in hydrogen. $C_1$ through $C_8$ are coincidence circuits; $D_1$ through $D_8$ are discriminators. M is a multichannel circuit in which individual counter pulses were mixed for display on an oscilloscope.

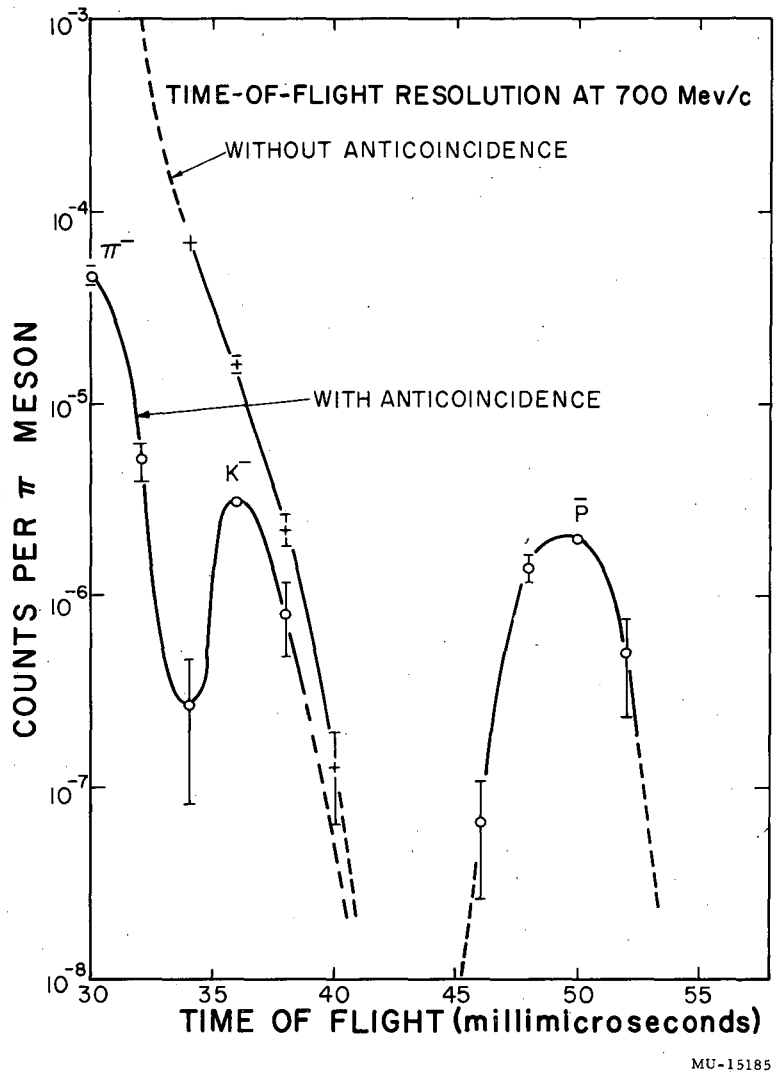


Fig. 6. Delay curve for time-of-flight counters. Curves with and without a time-of-flight anticoincidence pulse show rejection of background due to fast particles. The ordinate is normalized to the number of fast particles in the beam measured without the anticoincidence counter pulse. The abscissa is the cable delay between counters A and F.

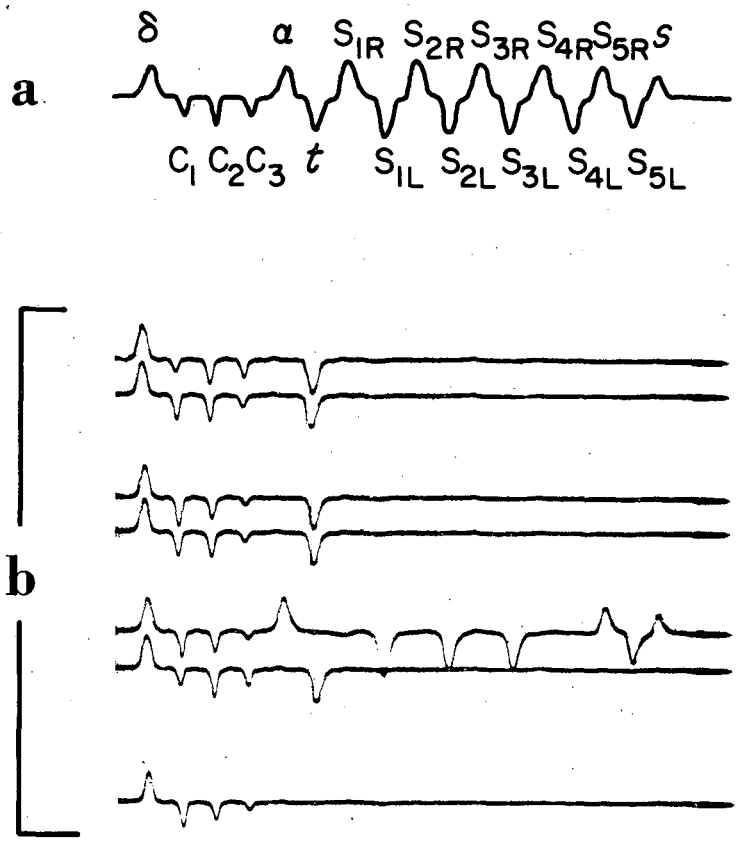


MU-15491

Fig. 7a. Drawing of oscilloscope trace showing all possible pulses. Pulses a, t, $S_1$—$S_5$, and s are explained in text; δ is the antiproton gate; and $C_1$, $C_2$, and $C_3$ are pulses from a three-channel chronotron which gives an accurate time-of-flight measurement.

7b. Oscilloscope record showing 30 seconds of "typical" operation (800 Mev/c). Five of the traces show an antiproton transmitted by the hydrogen target (no interaction). The fifth trace from the top shows an annihilation into at least six secondaries, while the last trace shows a charge exchange (no count in a, t, or s).

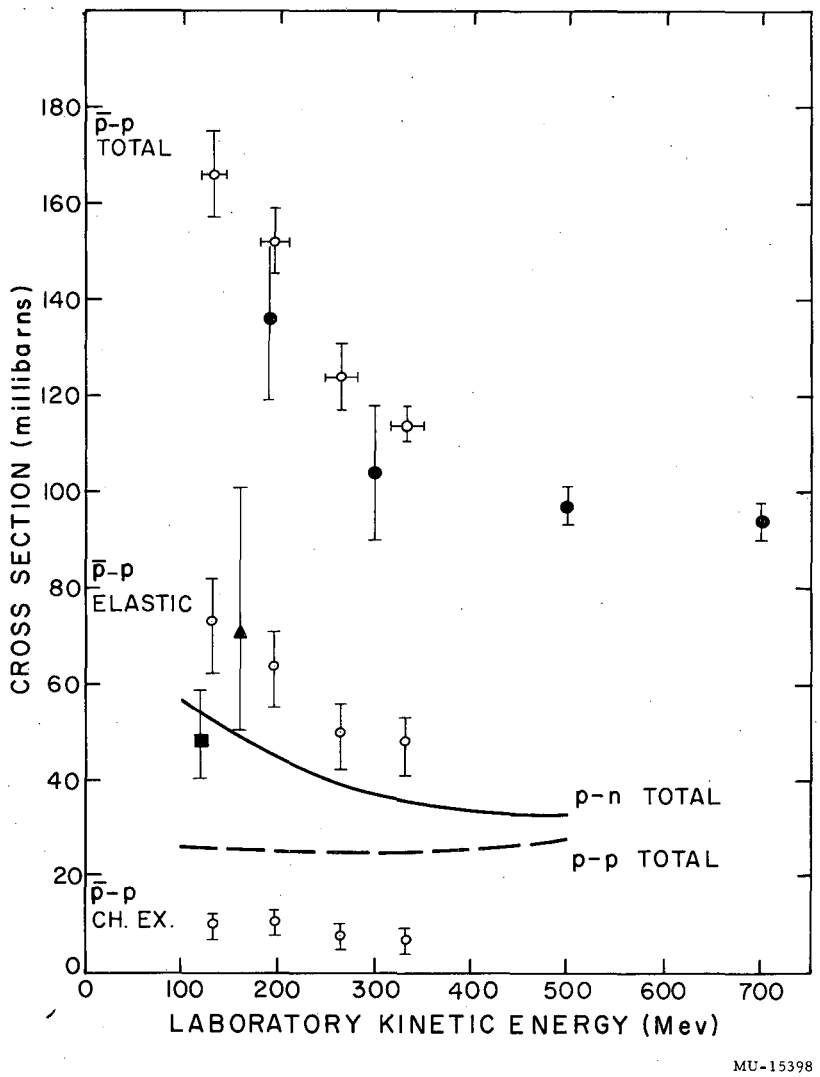


Fig. 8. Energy dependence of total, elastic, and charge-exchange $\bar{p}$-p cross sections. Results of this experiment are indicated by open circles. The solid circles are total cross sections from Ref. 1; the solid triangle (from Ref. 4) and the solid square (from Ref. 3) are for elastic scattering cross sections. (For the last point we have made a 7-mb forward-scattering correction.) For convenient reference, p-p and p-n total cross sections in the same energy range are shown. The indicated uncertainties are discussed in the text, and are both statistical and instrumental in origin.

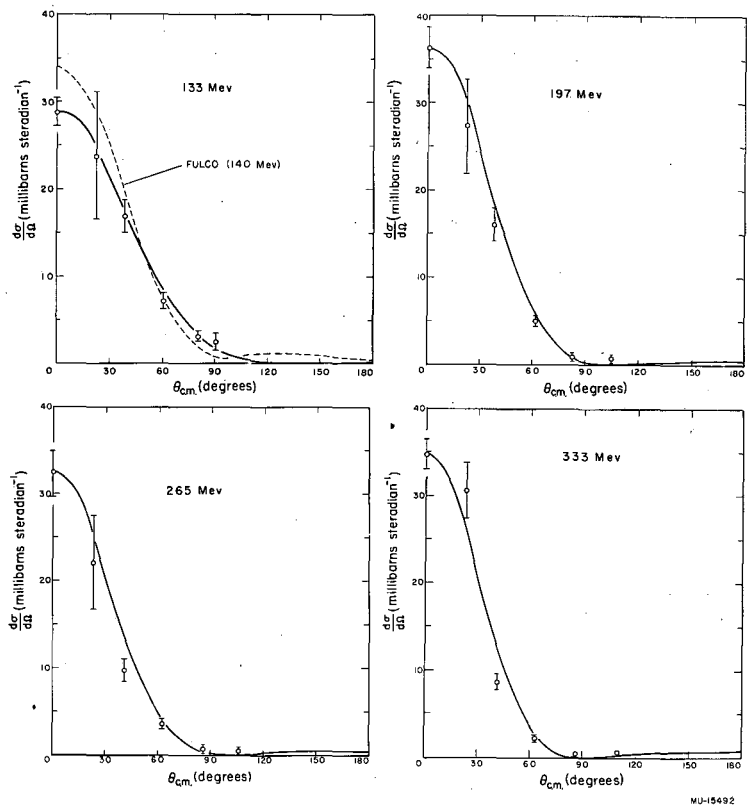


Fig. 9. Angular distributions of the elastic scattering at four energies. The point at $\theta = 0$ was obtained from the measured total cross section with the help of the "optical theorem." It is a minimum value, as is predicted for a purely absorptive interaction. The solid curves are obtained with the help of the optical model for a classical "black sphere" interaction. Indicated uncertainties are statistical only. The dashed curve labeled FULCO is from Ref. 7.

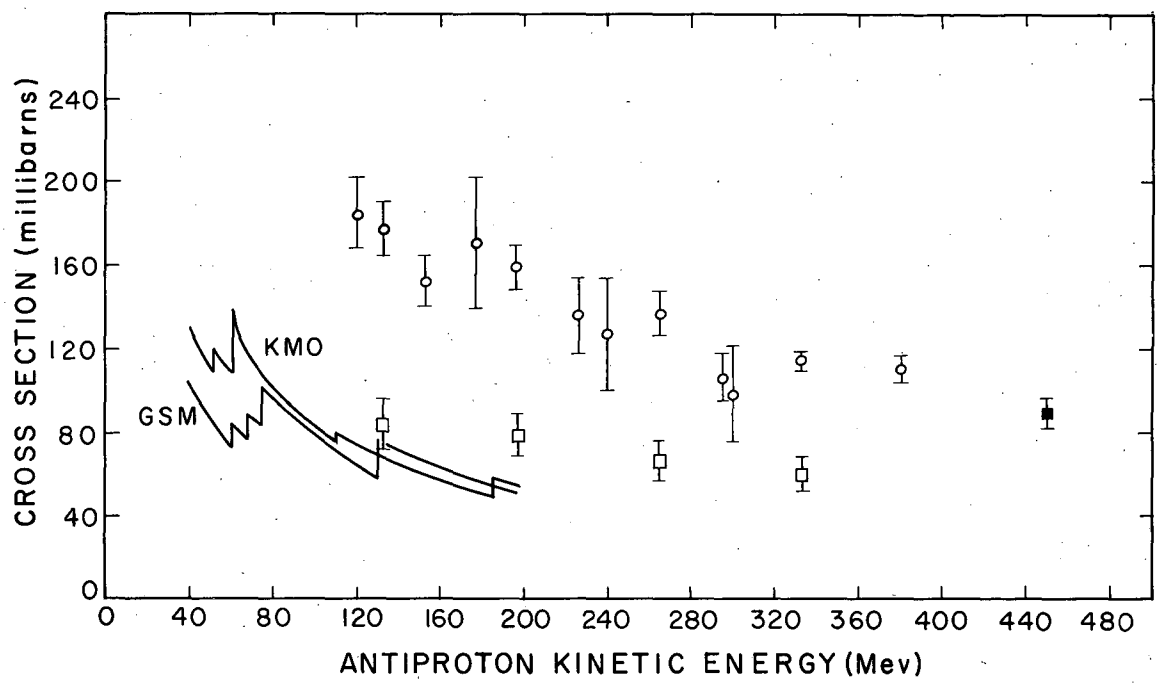


MU-15,397

Fig. 10. Energy dependence of total and inelastic $\bar{p}$-p cross sections. For each of the four energies represented in Fig. 8 the total-cross-section data were subdivided into three energies with the help of the chronotron information. The uncertainties indicated for the total-cross-section points (open circles) are statistical only. The inelastic cross section is indicated by open squares. Uncertainties are discussed in the text. The solid square is an annihilation cross section from Ref. 2. The solid curves, from Ref. 6, represent theoretical energy dependences of the inelastic cross section for two potentials which give correctly the p-p and p-n cross sections in this energy range.